



A full-vector paleomagnetic record from the southern South China sea reveals regional geomagnetic instability over the past 30,000 years

Shuang Wu^a, Tingwei Zhang^{a,b,*}, Xiaoqiang Yang^{a,**}, Shiyu Zhu^a, Shengtan Shang^a, Yulan Ye^a

^a School of Earth Science and Engineering/Guangdong Provincial Key Laboratory of Geodynamics and Geohazards, Sun Yat-sen University, Guangzhou, China

^b State Key Laboratory of Lithospheric and Environmental Coevolution, Institute of Geology and Geophysics, Chinese Academy of Sciences, Beijing, China

ARTICLE INFO

Handling Editor: Biagio Giaccio

Keywords:

Paleosecular variation
West Pacific anomaly
Late Pleistocene

ABSTRACT

The Western Pacific Anomaly (WPA), a low-intensity geomagnetic anomaly associated with complex geodynamic processes, remains poorly understood due to the limited availability of paleomagnetic records from the region. Here, we present a high-resolution full-vector paleomagnetic record from core BKAS58PC in the southern South China Sea, spanning the past 30,000 years and filling a critical gap in Late Pleistocene geomagnetic records from the equatorial western Pacific. The directional data reveal multiple large-amplitude geomagnetic directional swings between 30 and 10 ka, reflecting axial dipole instability during the post-Mono Lake excursion recovery phase. Comparisons with regional and global paleointensity records reveal pronounced differences in behavior, particularly between 30 and 23 ka, indicating enhanced non-dipole activity and possibly the recurring emergence of the WPA. Our findings provide a rare constraint on geomagnetic variability in the equatorial western Pacific and may offer new insights into the Earth's interior dynamics.

1. Introduction

In recent years, growing attention has been directed toward the evolution of geomagnetic non-dipole fields, largely due to the continued intensification of the South Atlantic Anomaly (SAA), which may indicate an impending geomagnetic reversal or excursion (Pavón-Carrasco and De Santis, 2016). This low-intensity geomagnetic feature, associated with reverse flux patches at the core-mantle boundary (CMB) (Campuzano et al., 2019), is hypothesized to be influenced by the African Large Low-Velocity Province (LLVP)—a substantial thermochemical anomaly structure in the lowermost mantle (Tarduno et al., 2015). Such structures are believed to be long-lived over million-year timescales, potentially facilitating the recurrent occurrence of geomagnetic anomalies in spatially consistent regions (de Oliveira et al., 2024; Engbers et al., 2024; Terra-Nova et al., 2015, 2016, 2019). While studies of the SAA have improved our understanding of non-dipole field dynamics, relying on a single anomaly may hinder a more comprehensive global perspective. The only other recognized anomaly—the Western

Pacific Anomaly (WPA)—has, however, received far less attention and remains poorly understood due to limited reliable records (Jackson et al., 2000).

The WPA was first identified in gulfm1 geomagnetic field model during the 17th–18th centuries and further corroborated by historical records and equatorial auroral observations (Campuzano et al., 2019; He et al., 2021; Jackson et al., 2000). Meanwhile, the western Pacific RPI stack (Dahrin et al., 2023; Yang et al., 2024; Zhong et al., 2020) over the past 30 kyr shows distinct deviations from records in the North Atlantic (Laj et al., 2000; Stoner et al., 2013) and global RPI records (Laj et al., 2004), particularly at ~7 ka, ~15 ka, and ~25 ka. These anomalies, together with regionally distinct low-intensity features in Holocene archaeomagnetic records, have prompted speculation about the possible recurrence of non-dipole sources in the equatorial western Pacific (Cai et al., 2021; Luo et al., 2025). However, significant challenges—including chronological uncertainties, remanence lock-in during sedimentation, and lithological or environmental influences—complicate the interpretation (Channell et al., 2020; Roberts and

* Corresponding author. State Key Laboratory of Lithospheric and Environmental Coevolution, Institute of Geology and Geophysics, Chinese Academy of Sciences, Beijing, 100029, China.

** Corresponding author. School of Earth Science and Engineering/Guangdong Provincial Key Laboratory of Geodynamics and Geohazards, Sun Yat-sen University, Guangzhou, 510275, China.

E-mail addresses: zhangtw6@mail.igcas.ac.cn (T. Zhang), esyxq@mail.sysu.edu.cn (X. Yang).

Winklhofer, 2004; Stoner et al., 2002). More high-quality regional paleomagnetic directional and intensity records are thus essential for reconstructing geomagnetic evolution at a regional scale.

The Late Pleistocene period following the Mono Lake excursion represents a key interval for investigating such non-dipole field activity, due to several regionally observed directional anomalies and marked differences in regional field intensity (Channell et al., 2020). However, paleomagnetic sediment records from the Western Pacific are scarce due to complex deglacial sedimentary processes and low sedimentation rates, which limit their resolution for capturing detailed field behavior. To date, core MD98-2181, recovered from the tropical Western Pacific Ocean, provides the only high-resolution full-vector record from this region during this period (Lund et al., 2017). The absence of additional comparative records limits the accuracy of geomagnetic field reconstructions in this region, restricting further investigation of the WPA. To help address these gaps, we present a high-resolution record of paleosecular variation from core BKAS58PC in the southern South China Sea, spanning the past 30 kyr. By comparing this record with other regional paleomagnetic data, we refine our understanding of geomagnetic variations over this critical interval and provide new perspectives on the regional manifestation of non-dipole field components and their geodynamic implications.

2. Materials and methods

The studied core BKAS58PC was collected from the southern South China Sea (112.0002°E , 6.932135°N) at a water depth of 2033 m using a gravity piston corer in June 2014 (Fig. 1a). The core with a length of 8.25 m was retrieved in a single pass and then cut into average 0.8-m sections on board. The sampling site, located on the distal part of the continental slope, is tectonically stable and flat, with sediment primarily sourced from the Mekong River estuary, Borneo and nearby islands (Liu et al., 2013; Zhang et al., 2007). The sediment lithology is relatively homogeneous, dominated by light gray clay with occasional fine silt interlayers.

After magnetically shielded transport and preservation, the core was split in the sampling laboratory along its central axis. After scraping off the thin layer of sediment disturbed by cutting on the split-core surface, a total of 414 cubic samples ($2 \times 2 \times 2\text{ cm}$) were extracted continuously along the axis of the core for paleomagnetic and anisotropy of magnetic susceptibility (AMS) tests, with paired powder samples collected for environmental and rock magnetic analyses.

The AMS was measured for each specimen using a KLY-5 Kappabridge system (976 Hz, 200 A/m) prior to conducting demagnetization experiments. Natural remanent magnetization (NRM) and stepwise alternating field (AF) demagnetization were then performed using a 2G-760 superconducting rock magnetometer with peak magnetic fields

ranging from 0 to 80 mT and steps of 10 mT. Anhysteretic remanent magnetization (ARM) was acquired with a 0.05 mT DC field superimposed on an 80 mT AF field. Saturation isothermal remanence (SIRM) and reverse-field isothermal remanence were imposed with a DC field of 1 T and -300 mT (IRM_{300mT}). Both SIRM and ARM were subsequently demagnetized using AF steps identical to those applied to NRM.

Temperature-dependent magnetic susceptibility curves ($\chi\text{-T}$) were measured in an argon atmosphere using a KLY-5 Kappabridge equipped with a CS-3 furnace. Low-temperature magnetic experiments, including zero-field cooling (ZFC) and field cooling (FC) measurements were performed in a vibrating sample magnetometer (VersaLab) with a maximum DC field of 3 T over a temperature ranging from room temperature to 50 K. Temperature-dependent magnetizations ($M_s\text{-T}$) were measured in argon atmosphere with a DC field of 1 T using Lake Shore 8604 vibrating sample magnetometer equipped with an SSVT system at Joint International Research Laboratory for Environmental and Social Archaeology, Shandong University.

Magnetic hysteresis properties and first-order reversal curve (FORC) diagrams were measured for representative samples using a MicroMag 3900 vibrating sample magnetometer with a maximum applied field of 1 T. Hysteresis loops were obtained with 10 mT field increments and parameters including saturation magnetization (M_s), saturation remanence (M_{rs}), and coercivity (B_c) were calculated after high-field slope correction for the paramagnetic contribution. The coercivity of remanence (B_{cr}) was determined from the demagnetization curve of the remanence. The FORC grid comprised 150 hysteresis loops with an averaging time of 1 s per measurement, and the data were processed using FORCinel 3.06 software with a smoothing factor of 7 (Harrison and Feinberg, 2008).

Magnetic minerals were extracted from representative samples using a bar magnet, dispersed in anhydrous ethanol, and drop-cast onto silicon wafers before being air-dried. The mineralogical characteristics were then analyzed using scanning electron microscopy (SEM) coupled with energy dispersive X-ray spectroscopy (EDS) at the Southern Marine Science and Engineering Guangdong Laboratory (Zhuhai). All demagnetization experiments were conducted at the Environmental Magnetism Laboratory, China University of Geosciences (Wuhan), while other rock magnetic analyses were completed at the Magnetism Laboratory, School of Earth Science and Engineering, Sun Yat-sen University.

Additionally, planktonic foraminifera fossils from 16 samples were selected for radiocarbon dating. The sediments were first treated with 10% hydrogen peroxide for 36 h to remove organic matter, followed by sieving to isolate the $> 0.063\text{ mm}$ fraction. Cleaned planktonic foraminifera were then picked under a microscope and sent to Beta Analytic Laboratory for accelerator mass spectrometry radiocarbon dating.

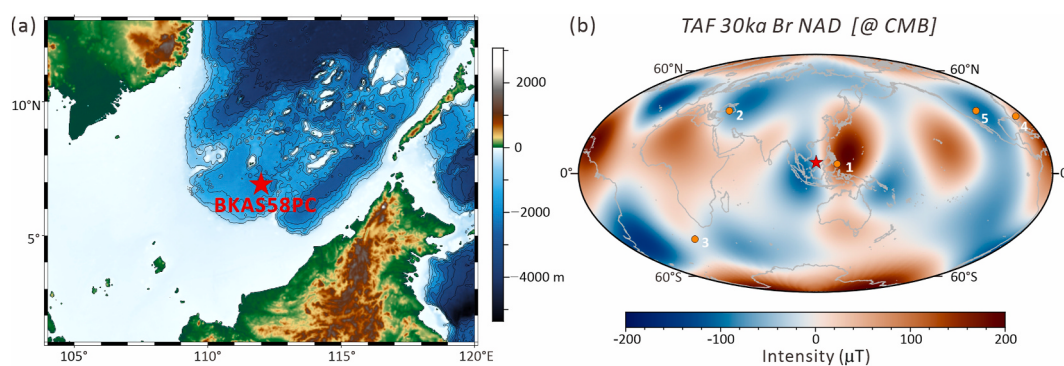


Fig. 1. Location of core BKAS58PC (red star). (a) Geographic position and water depth of the drilling site. (b) Time-averaged field (TAF) of the radial component (B_r) of the non-axial-dipole (NAD) field at the CMB over the past 30 kyr, derived from GGF100k model with 200 year interval (Panovska et al., 2018). Orange dots indicate sites or projection points of stack records referenced in this study: 1 - MD98-2181 (Lund et al., 2017), 2 - Black Sea stacks (Nowaczyk et al., 2013), 3 - TTN-057-5-PC01 (Channell et al., 2000), 4 - CH88-10P (Lund et al., 2005), 5 - WNAM17 stacks (Reilly et al., 2018).

3. Results

3.1. Age model

The radiocarbon dating results for planktonic foraminifera from 16 selected samples are presented in Table S1. The radiocarbon ages were calibrated using the Marine 20 calibration curve (Heaton et al., 2020) in Calib 8.1 software (Stuiver and Reimer, 1993). A local marine reservoir correction (ΔR) of -157 ± 33 years was applied, derived by averaging values from nearby reference sites in the global marine reservoir ($n = 8$) (Reimer and Reimer, 2001). An age-depth model spanning the past 30 kyr was constructed using Undatable software with parameters set to $x\text{factor} = 0.1$ and $\text{bootpc} = 30$ (Fig. 2). The $x\text{factor}$ scales the width of the Gaussian distribution, while bootpc determines the percentage of age-depth constraints to be bootstrapped in each iteration (Louheed and Obrochta, 2019). Sediment accumulation rate (SAR) was estimated by multiple model simulations, accounting for uncertainties in both age and depth. The median SAR for core BKAS58PC indicates lower deposition rates during the Holocene and Last Glacial Maximum, ranging from 10 to 30 cm/kyr, while during the Last Deglaciation (22–13 ka) the rate peaks at a maximum of 110 cm/kyr.

3.2. Anisotropy of magnetic susceptibility

Anisotropy measurements were conducted to examine the sedimentary fabric and assess potential disturbances to the paleomagnetic signal. The results indicate that the maximum (K_{\max}) and intermediate (K_{int}) axes are oriented horizontally, with a random distribution near the periphery of the projection circumference (Fig. S1). The minimum axes (K_{\min}) are nearly perpendicular to the bedding plane, concentrated at the center of the projection diagram. Magnetic lineation (L) values are < 1.02 and smaller than magnetic foliation (F), with the degree of anisotropy (P) ranging from 1.00 to 1.08, exhibiting a strong linear correlation with F . These characteristics define an oblate magnetic

susceptibility ellipsoid, suggesting an undisturbed primary sedimentary fabric (Tarling and Hrouda, 1993).

3.3. Magnetic properties of sediments

Magnetic susceptibility (χ), SIRM, and ARM exhibit generally consistent trends below 1 m depth, with ARM showing greater variability probably due to its enhanced sensitivity to fine-grained minerals (Dunlop and Özdemir, 1997) (Fig. 3). Between 8.25 to 6.6 m, magnetization progressively weakens upward, likely reflecting a reduction in magnetic mineral concentration. Pronounced magnetization decreases, accompanied by abrupt S_{300} ratio increases, occur in the 6.6–5.9 m and 5.5–5.3 m intervals, where FORC diagrams display noisy pseudo-single domain (PSD) characteristics. Between 5.9 and 5.5 m, magnetic enhancement is indicated by concurrent increases in SIRM/ χ and S_{300} , along with concentric FORC contours diagnostic of greigite (Roberts et al., 2011), likely reflecting diagenetic alteration within these layers. Above 5.3 m depth, sediments exhibit enhanced magnetic properties and lower S_{300} ratio, dominated by stable single-domain (SD) particles with minimal variability. However, in the uppermost 1 m, an inverse correlation between remanence and susceptibility is observed, with elevated SIRM/ χ and higher ARM indicating a relative upward increase in SD grain contribution toward the top (Dunlop and Özdemir, 1997).

Further rock magnetic analyses were performed on selected samples to determine their minerals. The χ -T heating curves show an increase near 300 °C in some samples, most notably at 5.81 m, possibly suggesting thermal alteration of iron sulfides into ferrimagnetic phases (Fig. 4a). All samples display a pronounced susceptibility decrease near 580 °C, indicating magnetite, though enhancements on the cooling curves suggest additional magnetite formation during heating. To further clarify the source of the magnetite signal, low-temperature magnetic measurements were conducted. The results confirm that, except for the 5.81 m sample, all specimens exhibit a Verwey transition between 90 and 120 K, consistent with primary magnetite (Fig. 4c).

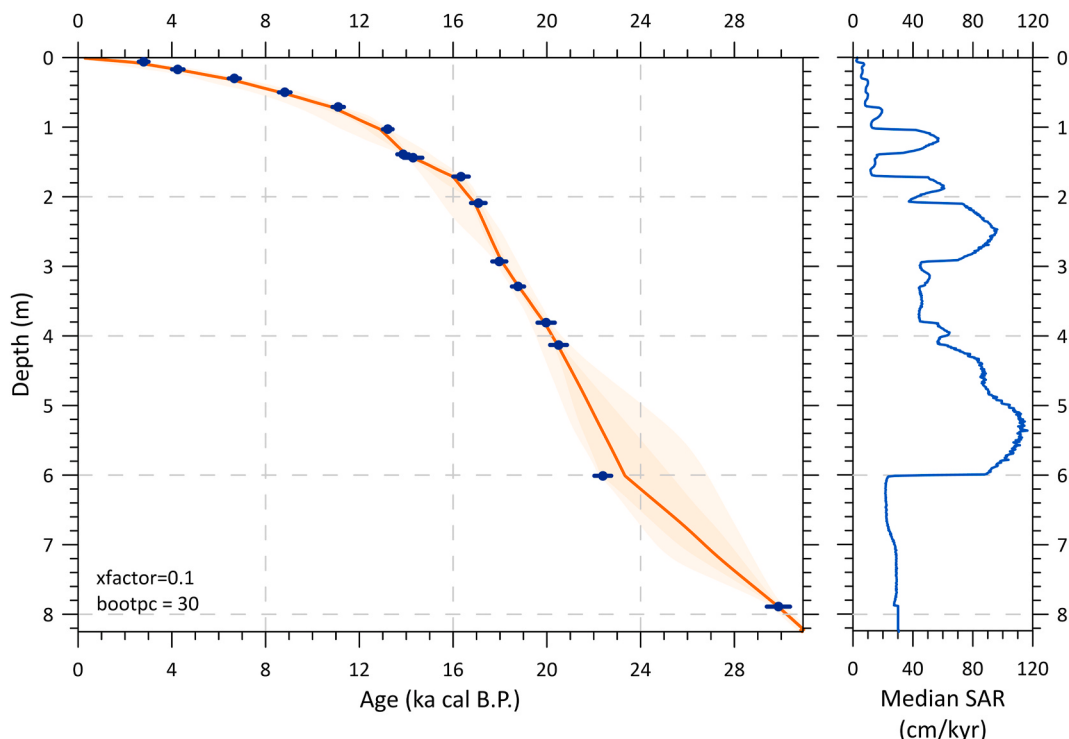


Fig. 2. Age model of core BKAS58PC. Calibrated radiocarbon ages are indicated by blue dots, with error bars representing 2σ uncertainties. The 1σ and 2σ uncertainties of the age model are shown as dark and light orange shading, respectively. The variation of median sediment accumulation rate (SAR) with depth is shown plotted on the right.

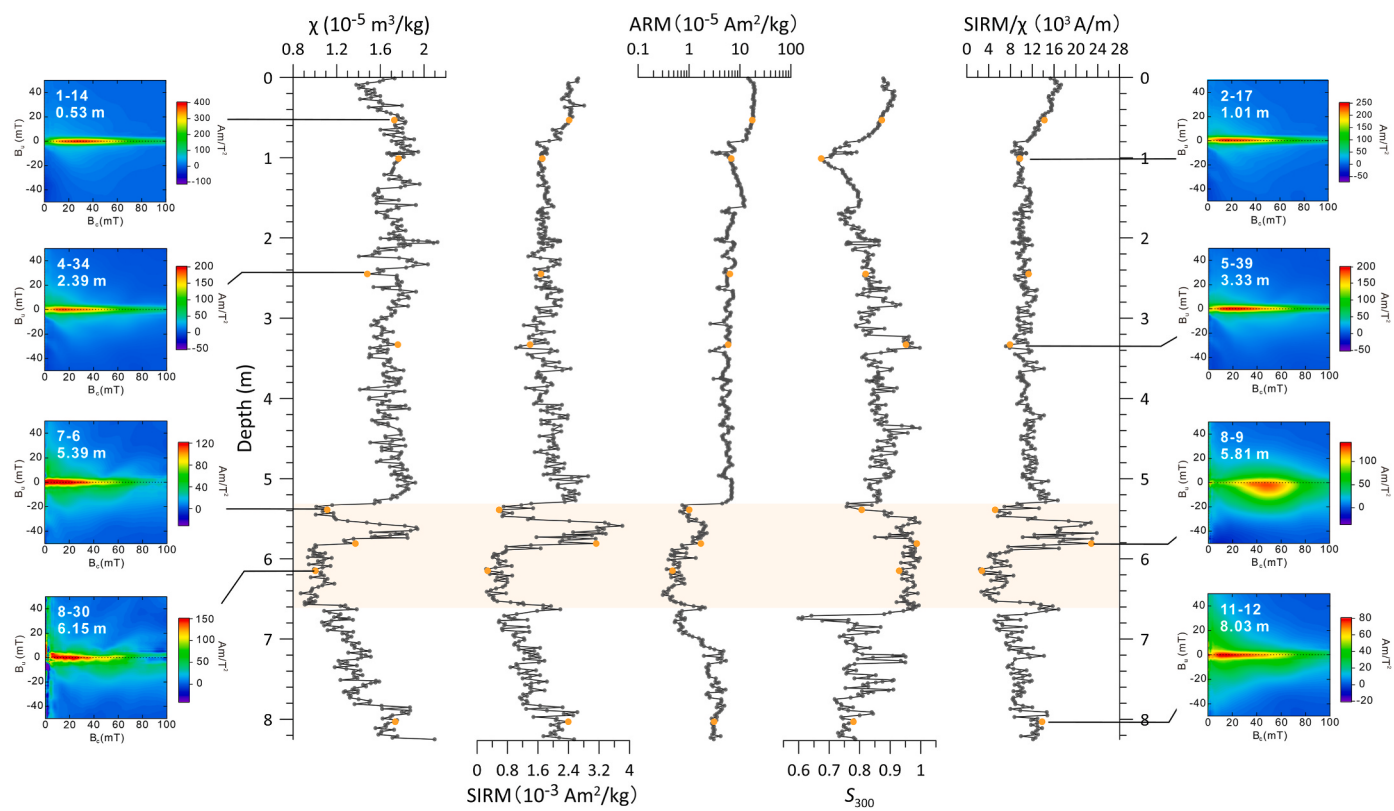


Fig. 3. Variation of susceptibility (χ), SIRM, ARM, S_{300} and S_{300}/χ , with FORC diagrams from specific layers. The S_{300} is defined as the ratio of IRM_{300mT} and SIRM. Samples used for rock magnetic testing are indicated by orange dots. The interval potentially affected by diagenesis is highlighted by orange shading.

Slightly lower transition temperatures may reflect contributions from minor cation substitutions or biogenic magnetite (Jackson and Moskowitz, 2021).

M_s -T measurements under an argon atmosphere for two high-coercivity samples show gradual magnetization loss above 600 °C, indicative of hematite (Fig. 4b). However, no distinct Morin transition was observed in the low-temperature magnetic curves, likely due to the small grain size, low abundance, or poor crystallinity of hematite, all of which are known to suppress this transition (Dunlop and Özdemir, 1997). Some hysteresis loops remained open at 500 mT, implying the presence of even higher-coercivity phases (Fig. S2). Hysteresis loops and Day plot analysis (Dunlop, 2002) indicate a dominance of SD-PSD behavior, consistent with observations from FORC diagrams. High-coercivity minerals typically shift Day plot data toward higher B_{cr}/B_c and M_r/M_s values (Dunlop, 2002). However, in our samples, this effect is minimal, indicating that these phases are present but do not dominate the magnetic signal.

IRM component analysis (Fig. S3) shows that the remanence of representative samples is carried by three components: low-coercivity (~20 mT), middle-coercivity (55–70 mT), and high-coercivity (>400 mT). The low-coercivity component is interpreted as representing primary detrital magnetite or biogenic magnetite (Egli, 2004). The dominant middle-coercivity component is likely attributed to partially oxidized detrital magnetite (Necula et al., 2024; Sakuramoto et al., 2017; Yamazaki et al., 2023). Such minerals are plausibly derived from soils in the Mekong Basin and surrounding tropical islands, where high precipitation and elevated temperatures promote intense chemical weathering and efficient fluvial transport (Li et al., 2018; Oliva et al., 2003). In addition, a fraction of magnetite with elevated coercivity, likely resulting from Ti substitution, may also be present. The high coercivity component exhibits a wide dispersion and is likely derived from, though not limited to, hematite. Variations in the abundance of this component primarily drive the observed S_{300} fluctuations, yet its

contribution to the bulk remanent magnetization remains generally below 15%.

Collectively, these magnetic signatures indicate an assemblage dominated by partially oxidized detrital magnetite exhibiting SD-PSD behavior in most layers, accompanied by unoxidized magnetite and minor high-coercivity phases. Evidence indicates diagenetic alteration between 6.6 and 5.3 m, during which dissolution of fine single-domain iron oxides attenuated the magnetization and promoted localized authigenic pyrite and greigite formation near 5.8 m.

SEM and EDS analyses confirm the distribution of magnetic minerals (Figs. 5 and 6). The 8.03 m sample shows considerable variation in grain size, with SD-sized iron oxides embedded within coarse-grained iron-bearing silicates, acting as the dominant magnetic carriers (Fig. 5k and l). At 5.81 m (a strong magnetization zone), frambooidal pyrite aggregates composed of octahedral single crystals are observed (Fig. 5g and h). These pyrite particles (>20 µm) are characteristic products of early diagenesis under oxygen-depleted conditions, with greigite likely forming as an intermediate phase preserved within incompletely transformed pyrite aggregates (Wilkin et al., 1996; Wilkin and Barnes, 1997). Nevertheless, some detrital magnetic minerals are preserved and may retain primary paleomagnetic signals (Fig. 5i and j). At 5.39 m (a weak magnetization zone), micron- to submicron-sized magnetic particles are detected, with some larger grains showing signs of partial dissolution (Fig. 5e and f). No iron sulfides were detected; only non-magnetic sulfate minerals were present, indicating an early diagenetic stage characterized by active iron reduction but preceding substantial sulfate reduction. The upper layers (1.01 m and 2.39 m) contain abundant PSD-SD-sized magnetite with sharp-edged octahedral morphologies and no evidence of dissolution (Fig. 5a–d). EDS analysis identifies these particles as iron oxides, some of which contain Ti, confirming their identity as well-preserved magnetic carriers. These observations are consistent with rock magnetic data and collectively confirm the preservation of detrital magnetite.

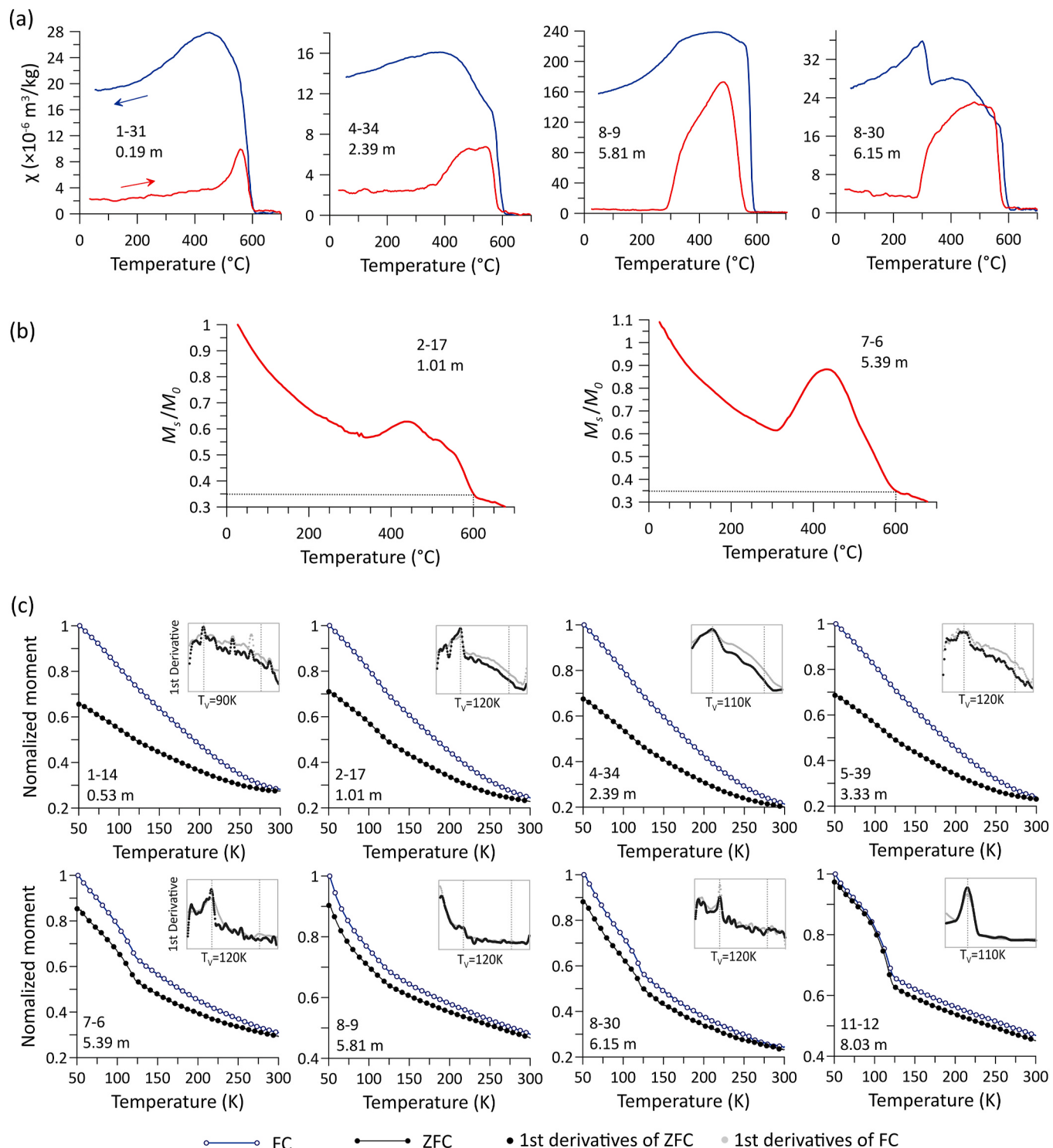


Fig. 4. Temperature-dependent magnetic properties of representative samples. (a) χ -T curves measured during heating (red) and cooling (black) cycles. (b) M_s -T heating curves; the dashed line indicates the saturated magnetization at $600\text{ }^{\circ}\text{C}$. (c) ZFC (black) and FC (blue) magnetization curves, with their first derivatives (ZFC: black; FC: gray) shown in the inset. Dashed lines in the inset highlight peaks between 90 and 120 K associated with the Verwey transition. The absence of features near 250 K suggests no detectable Morin transition.

3.4. Variations of full-vector geomagnetic components

Fig. 7 illustrates orthogonal vector projections of demagnetization for representative samples. With the exception of the 5.69 m sample, all specimens exhibit stable remanence directions decaying toward the origin. Components above AF 50 mT show no deviation from the low-coercivity fraction, indicating that the middle-coercivity minerals are

also capable of recording geomagnetic directional signals as the primary magnetite. Meanwhile, most samples lost $\sim 90\%$ of their magnetization by AF 80 mT , suggesting that high-coercivity minerals do not significantly influence AF demagnetization results for most layers. Characteristic remanent magnetization (ChRM) directions were determined using principal component analysis (Kirschvink, 1980) based on at least five consecutive demagnetization steps showing linear decay. In cases of

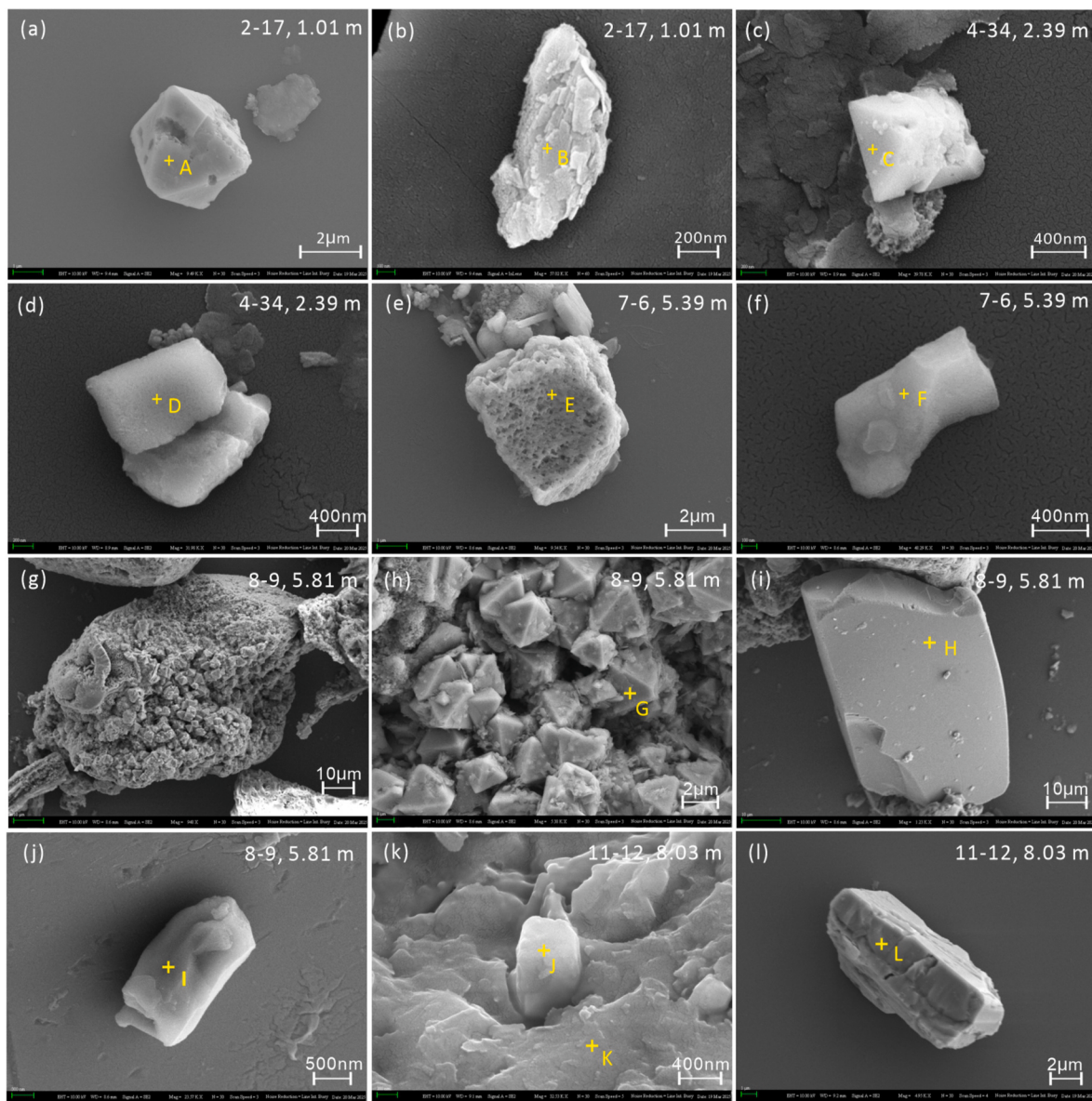


Fig. 5. SEM micrographs of representative specimens. The micrographs were acquired in SE2 mode (secondary electron imaging using an Everhart-Thornley detector) at 10 kV. Designated points (A–L) indicate locations subjected to EDS elemental analysis, with corresponding elemental spectra presented in Fig. 6.

directional instability, we preferentially used the component isolated at lower demagnetization fields between 20 and 50 mT. Only directions with maximum angular deviation (MAD) values $< 6^\circ$ were considered reliable and included, thereby excluding samples with ambiguous demagnetization behavior likely affected by high-coercivity components or secondary overprints.

For the 5.69 m sample, which contains greigite based on rock magnetic evidence, a noticeable gyroremanent magnetization (GRM) was observed above AF 50 mT. Nonetheless, the low-coercivity component exhibited a well-defined linear decay toward the origin. This interval was isolated as the ChRM, and the result was retained for further evaluation. The final ChRM directions and associated uncertainties are presented in Fig. 8. The declination values were obtained by adjusting the core-top declination to the modern field value and aligning the average of three samples at the segment junctions, reflecting relative changes rather than absolute values.

RPI was estimated by normalizing NRM loss within the 20–50 mT demagnetization range to the corresponding decrease in SIRM over the same interval. Results of NRM normalized by susceptibility, ARM, and

SIRM are shown in Fig. S4. The ARM-normalized series deviates substantially from the others, likely because ARM is highly sensitive to fine grain sizes and magnetostatic interactions (Dunlop and Özdemir, 1997; Yamazaki and Ioka, 1997; Yamazaki and Kanamatsu, 2007), showing variations exceeding an order of magnitude in core BKAS58PC and falling outside the criteria for reliable RPI estimation (Tauxe, 1993). The susceptibility- and SIRM-normalized results are generally consistent; however, as susceptibility often carries more complex signals while SIRM is less affected by such factors (e.g., grain size changes), SIRM was chosen as the normalizer.

In addition, Fig. 7 demonstrates that most samples exhibit stable, linear decay of remanence with consistent directions between 20 and 50 mT, carried by low-coercivity magnetite. Contributions from high-coercivity components or secondary overprints are minimal within this interval. Moreover, NRM/SIRM ratios derived from both individual demagnetization steps and the cumulative loss over the 20–50 mT interval show consistent trends (Fig. 9d), supporting the robustness and internal consistency of the chosen normalization approach. To further enhance the reliability of the RPI record and minimize potential bias

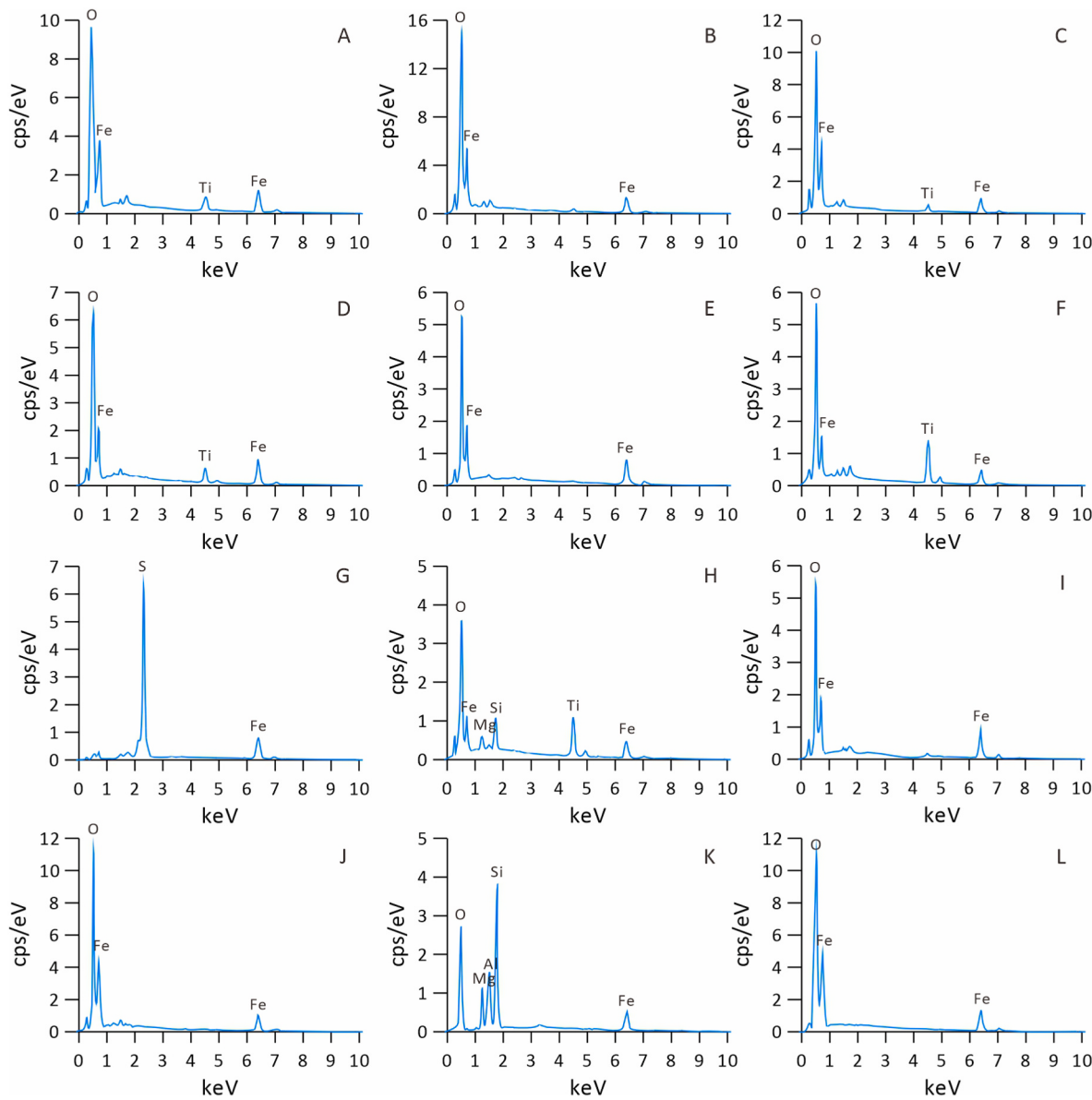


Fig. 6. EDS analysis with labeled characteristic peaks. Labels A-L correspond to marked positions in Fig. 5.

from high-coercivity phases or overprints, only samples with well-defined ChRM directions ($MAD < 6^\circ$) were included in the final dataset.

Although the estimated RPI shows limited correlation with $SIRM/\chi$ and the median destructive field (MDF) (Fig. 9a and b), which reflect variations in grain size and magnetic mineralogy, significant fluctuations in MDF are observed (Fig. 9e). To further minimize the potential influence, we applied a correction following the approach proposed by Brachfeld and Banerjee (2000), using the following equation:

$$RPI = (NRM_{20-50mT} / SIRM_{20-50mT}) \times (MDF_{CM} / MDF)$$

where MDF_{CM} is the center of mass of MDF, determined from the scatter plot of $NRM_{20-50mT}/SIRM_{20-50mT}$ vs. MDF (Fig. 9b). After applying the correction, the overall pattern of the RPI record remains largely unchanged (Fig. 9f). To evaluate the potential influence of concentration-related magnetic variations on the RPI estimates, cross-wavelet transform (XWT) and wavelet coherence (WTC) analyses were performed between $SIRM$ and RPI (Grinsted et al., 2004). The results show no significant correlation across the examined time and frequency domains (Fig. S5), indicating no coherent relationship between the two parameters. This further supports the robustness of the RPI estimates and their

independence from variations in magnetic mineral concentration. For the interval between 5.3 and 6.6 m, where rock magnetic results suggest possible diagenetic alteration, RPI values are retained for completeness but plotted as a dashed line in subsequent figures to indicate their tentative nature and the need for cautious interpretation.

4. Discussion

Over the past 30 kyr, paleomagnetic field reconstructions for the equatorial western Pacific have been limited by the lack of high-resolution, full-vector records, with core MD98-2181 being the only exception, which exhibits an average sedimentation rate of ~ 50 cm/kyr (Lund et al., 2006, 2017). Core BKAS58PC provides a rare, full-vector record from the southern South China Sea, with comparable average sedimentation rates of ~ 55 cm/kyr during the Last Glaciation, allowing for improved characterization of detailed regional geomagnetic variations. However, given the substantially lower sedimentation rates during the Holocene, which may obscure geomagnetic signals and introduce interpretive biases, the following discussion focuses primarily on paleosecular variation between 30 and 10 ka.

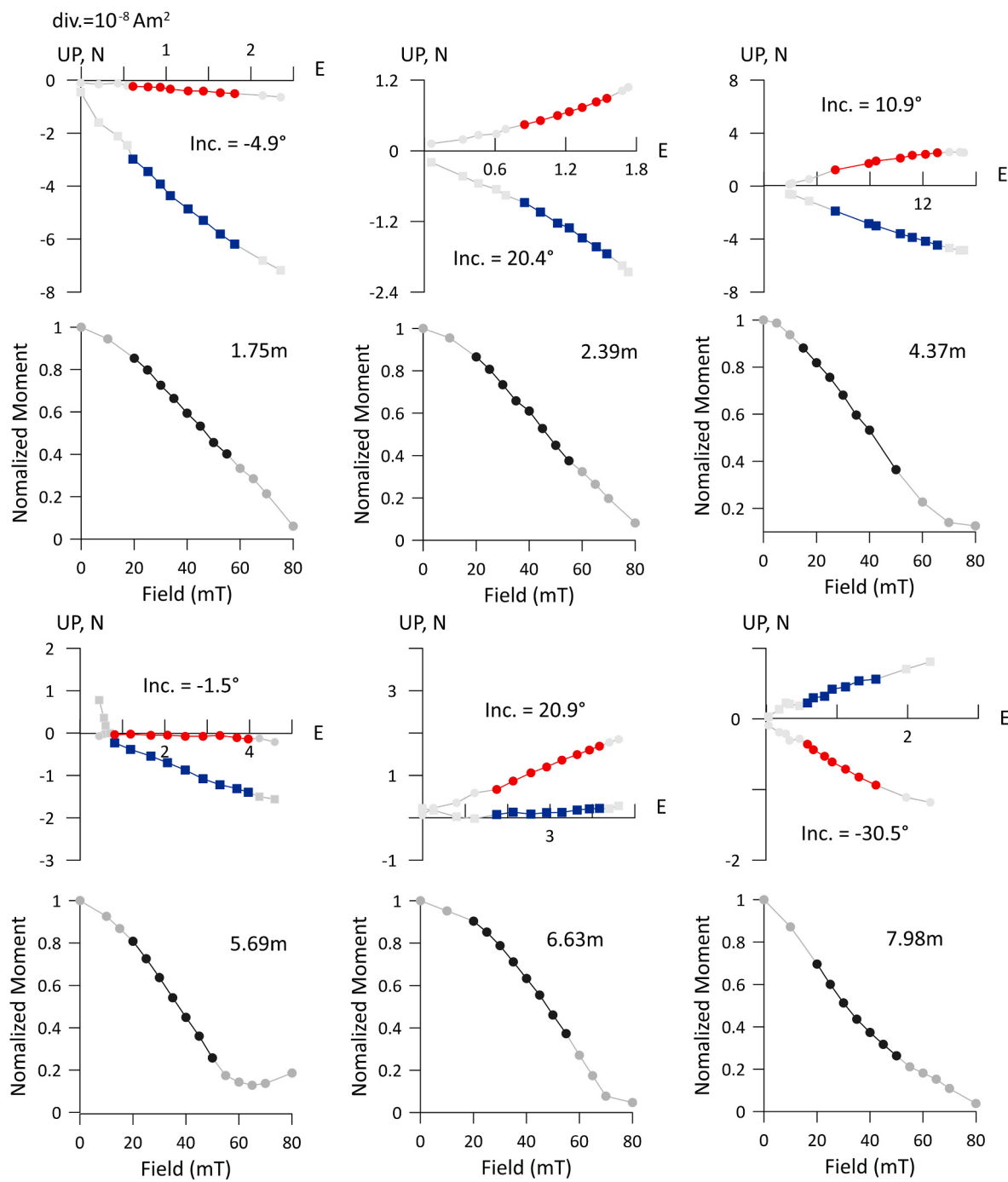


Fig. 7. Alternating field demagnetization results of representative specimens. Squares and circles indicate horizontal and vertical projections in vector component plots. Blue and red symbols denote data used to determine ChRM directions. Black circles represent normalized remanent magnetic moment for the alternating field. The derived inclination results are shown.

The inclination record of BKAS58PC exhibits a broadly consistent pattern with that of core MD98-2181 (Fig. 10), particularly regarding overall structure. Minor discrepancies at finer temporal scales may partly reflect smoothing effects related to differing sedimentation rates and uncertainties in age control. Nevertheless, both records capture pronounced inclination fluctuations between 30 and 26 ka, multiple oscillations between 22 and 18 ka, and two distinct shallowing events between 17 and 12 ka, collectively reinforcing the reliability of the BKAS58PC record.

Notably, the 25–23 ka interval, despite being affected by diagenetic processes, still exhibits directional variations closely matching those of

core MD98-2181. This similarity is likely due to the partial preservation of detrital magnetite throughout much of the interval, as supported by low-temperature magnetic measurements and SEM analyses. Newly formed ferrimagnetic minerals are restricted to a narrow age range between 23.1 and 22.6 ka. These greigite, capable of acquiring a chemical remanent magnetization at an uncertain time after deposition, may record a geomagnetic signal that is not coeval with the host sediment, thereby introducing temporal offsets (Roberts et al., 2011; Yang et al., 2022). However, based on the observed pyrite grain size in our samples, the greigite grains were likely formed during the early diagenetic stage, which would limit their influence on the paleomagnetic directions in

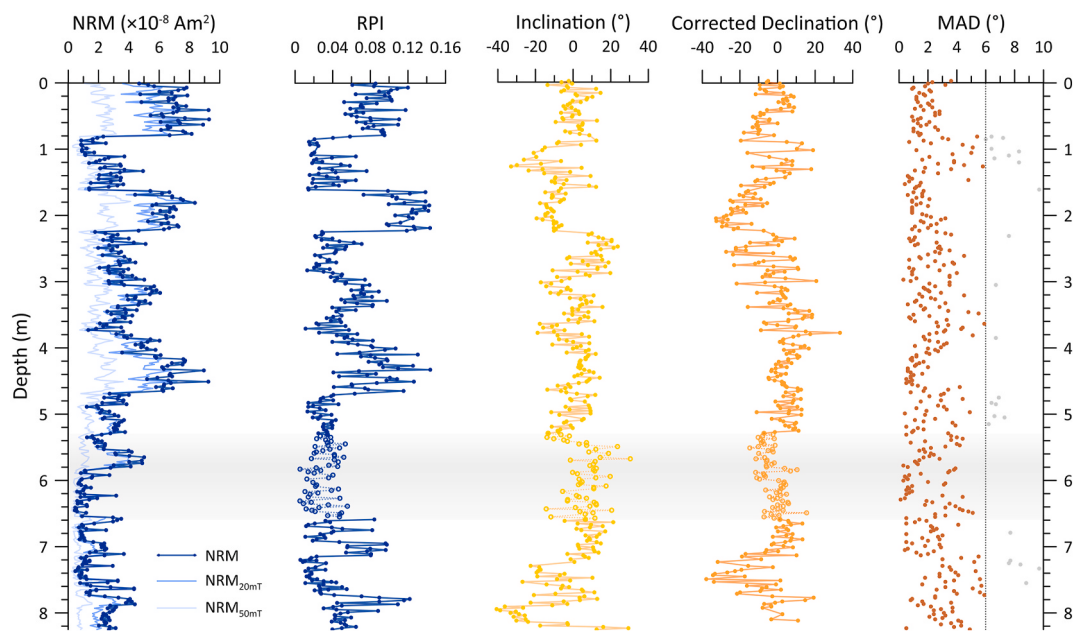


Fig. 8. Down-core plots of paleomagnetic results, including NRM, RPI, ChRM results, and their associated uncertainties. The interval potentially affected by diagenesis is indicated by hollow circle and dashed line, with gray shading highlighting the affected layers.

BKAS58PC; nonetheless, further investigations are needed to fully assess its potential impact.

Comparisons of paleosecular variation records from the Black Sea stack (Liu et al., 2018, 2019, 2022; Nowaczyk et al., 2013), Northwest American stacks (Reilly et al., 2018; Walczak et al., 2017), core 5-PC01 from the South Atlantic (Channell et al., 2000) and core CH88-10P from the North Atlantic (Lund et al., 2005) also show generally consistent patterns. Minor discrepancies may be attributed to chronological uncertainties and inherent smoothing effects during the acquisition of detrital remanent magnetization (Roberts and Winklhofer, 2004), as the chronologies of these records are generally based on oxygen isotope stratigraphy and lack independent radiocarbon age control. For instance, in the Black Sea record, directional fluctuations between 20 and 17 ka appear to have been smoothed into a broad low-inclination interval.

Of particular interest is the significantly larger inclination deviation (ΔI) observed in the Western Pacific–South China Sea region during 30–12 ka. ΔI is defined as the average difference between observed inclinations and those predicted by the Geocentric Axial Dipole (GAD) model (Johnson and Constable, 1995; Wilson, 1970). For stacked records, the coordinates refer to representative projection sites defined in the original publications (Liu et al., 2019; Reilly et al., 2018). While sediment compaction or drilling disturbance may have contributed to some inclination shallowing, the mean value of $\sim 9^\circ$ derived from normal polarity results differs from the 13.6° predicted by GAD by less than 5° , suggesting that such effects are limited and insufficient to account for the full amplitude of negative ΔI anomalies. Previous investigations of time-averaged geomagnetic fields over the past several thousand to million years have demonstrated a strong latitudinal dependence of ΔI , with larger negative values, approaching -10° , reported near the equator, particularly in the western equatorial Pacific (Elmaleh et al., 2001; Johnson and Constable, 1997; Lund, 2018; Yamazaki et al., 2008). Accordingly, we infer that a substantial portion of these anomalies likely reflects genuine geomagnetic behavior, associated with frequent displacements of the magnetic equator and enhanced non-dipole field activity in this region.

Nevertheless, the relative virtual geomagnetic pole (R-VGP) latitude calculated from inclination and corrected declination exhibits overall similarity to records from other regions, suggesting that VGP

movements during this period were still largely governed by the global dipole field (Fig. 11). The influence of regional non-dipole field components may have been more pronounced in the fine-scale morphology or amplitude of directional swings, rather than in the general trajectory of VGP changes.

Additionally, several low-latitude VGP features in our record may correspond to previously proposed excursion events, such as GGF-28k/Rockall (L5) (Channell et al., 2016; Panovska et al., 2018), Hilina Pali (L4–L2) (Laj et al., 2002; Peck et al., 1996), and Tianchi (L1) (Channell et al., 2020). The high-resolution BKAS58PC data capture finer-scale directional variations and reveal more detail than other low-resolution records. For instance, the Hilina Pali event appears to consist of multiple brief swings, potentially explaining its broad age range (22–16 ka) reported in earlier studies (Ahn et al., 2018; Liu et al., 2018; Nowaczyk et al., 2003; Singer et al., 2014; Yamazaki et al., 2003). These observations further suggest that following the Mono Lake excursion, when the global geomagnetic field intensity had not fully recovered, the field remained unstable and prone to frequent VGP movements (Yamazaki and Oda, 2002). However, none of these deviations appear to exhibit significantly larger amplitudes or clearly meet the criteria for a geomagnetic excursion (Laj and Channell, 2015). Whether they represent regional excursions or large-scale secular variation remains to be further investigated. Nevertheless, they can still serve as useful chronological tie-points for regional stratigraphic correlation.

In terms of paleointensity, the RPI record from core BKAS58PC exhibits a trend broadly consistent with that of core PC83 from the northern South China Sea (Yang et al., 2009), as well as with local field intensity values (F) simulated by the GGF100k model at the core site (Panovska et al., 2018) (Fig. 12). From 30 to 10 ka, the overall trend is increasing, punctuated by low-intensity intervals at 26–22 ka, 20–18 ka, and 15–12 ka. Notably, even during the 25–23 ka interval—potentially affected by diagenetic alteration—similarly low RPI values are observed, suggesting that these features may reflect genuine geomagnetic field behavior.

When compared with RPI records from the Black Sea (Nowaczyk et al., 2013), the South Atlantic (Channell et al., 2000), and the North Atlantic (Lund et al., 2005), as well as with the global dipole moment (GDM) reconstructed from ^{10}Be stacks of Greenland ice cores (Zheng et al., 2021), clear regional differences emerge during 30–23 ka. We

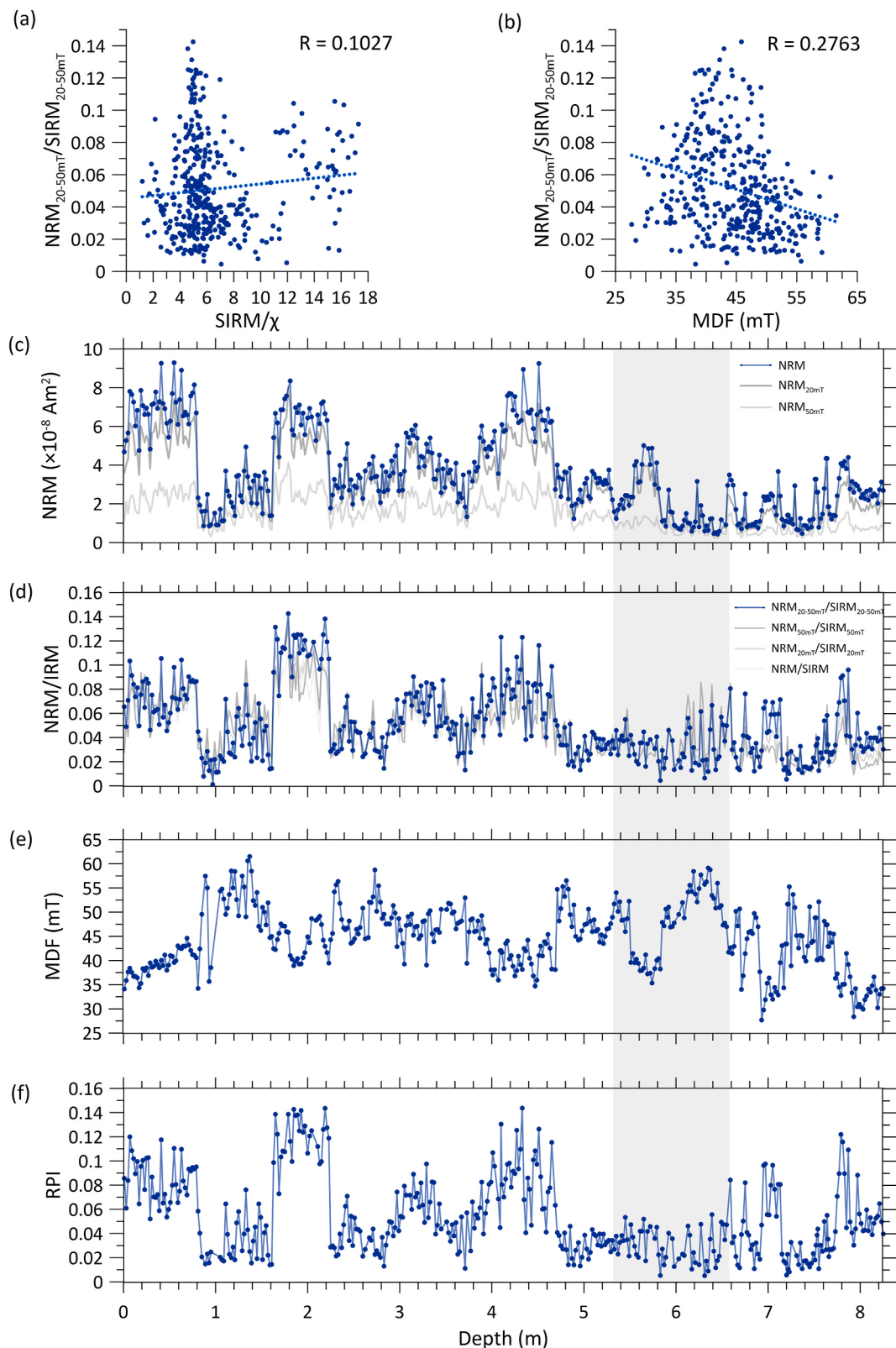


Fig. 9. Comparison of $NRM_{20-50mT}/IRM_{20-50mT}$ with $SIRM/\chi$ (a) and MDF (b), NRM at different demagnetization steps (c), NRM/IRM ratios calculated over various demagnetization intervals (d), MDF(e), and the final corrected RPI record (f). The gray-shaded interval denotes depths potentially affected by diagenesis.

propose that the influence of non-dipole fields was relatively enhanced during the period following the Mono Lake excursion, when the geomagnetic field intensity had not yet fully recovered. In contrast, between 22 and 12 ka, the convergence of regional and global intensity

trends, characterized by an overall strengthening and a similar strong-weak-strong pattern, suggests that as the axial dipole field recovered its strength, the influence of non-dipole contributions was reduced. Supporting this interpretation, the GGF100k model indicates that during

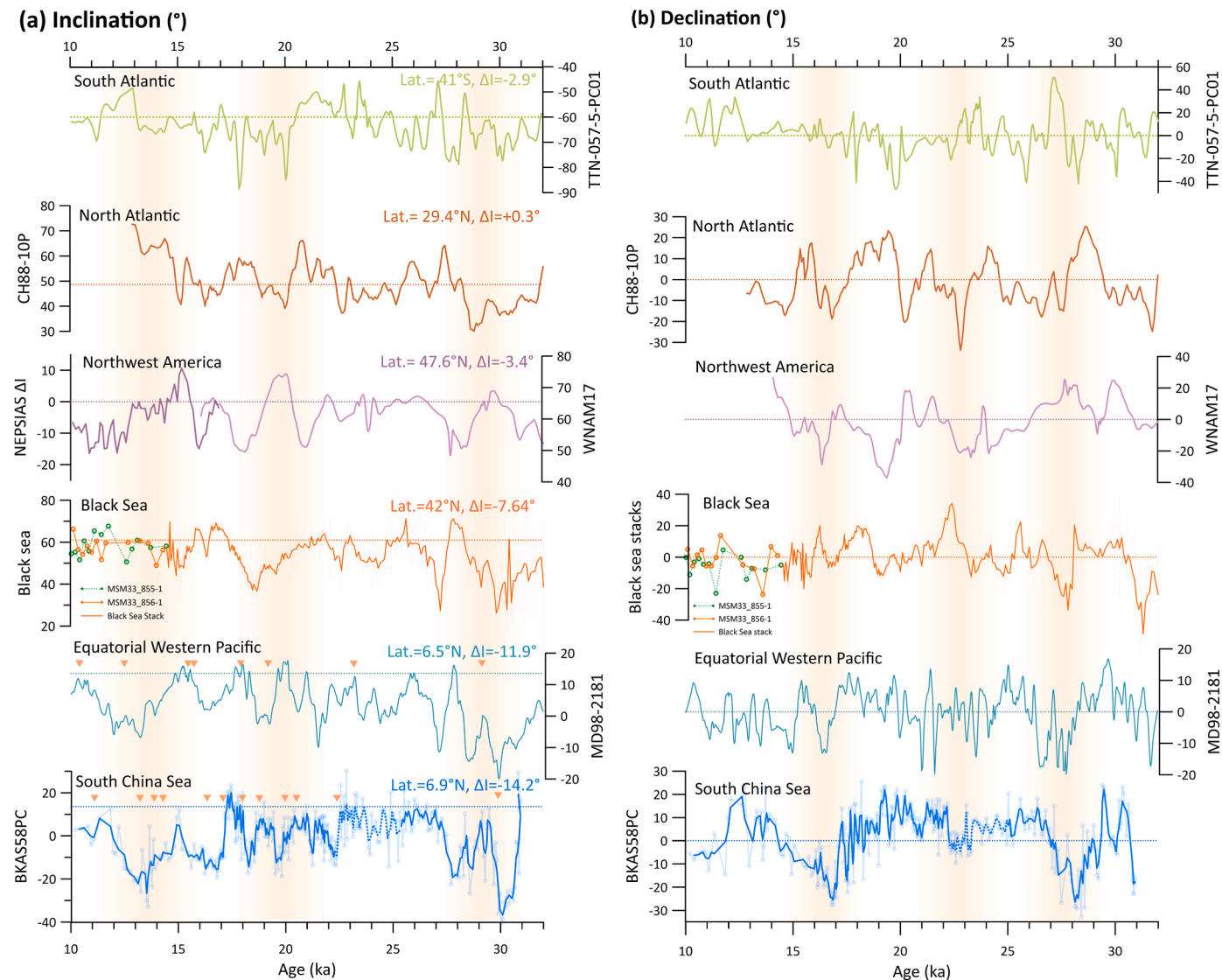


Fig. 10. Comparison of inclination (a) and declination (b) from BKAS58PC with records from other regions, including MD98-2181 (Lund et al., 2006, 2017), MSM 33_855-1 and MSM33_856-1 (Liu et al., 2022), Black Sea stack of 16 cores (Liu et al., 2020), NEPIAS (Walczak et al., 2017), WNAM17 (Reilly et al., 2018), 5-PC01 (Channell et al., 2000), and CH88-10P (Lund et al., 2005). Thick blue line shows a three-point moving average of the BKAS58PC results, with intervals of uncertain reliability denoted by dashed lines. GAD directions for each core are marked by dashed line. Calibrated AMS ¹⁴C ages from planktonic foraminifera are marked with orange inverted triangles. Orange bars indicate periods of pronounced geomagnetic directional variability.

30–28 ka and 25–21 ka, regional field intensities were significantly lower than the predicted axial dipole moment (ADM), reflecting a substantial negative contribution from non-dipole sources.

Combined with previous observations of significantly negative ΔI anomalies in the equatorial western Pacific, we propose that the enhanced non-dipole activity in the study area may be linked to the recurrent emergence of the WPA. The location of our core site corresponds to the position of the WPA observed during 1500–1900 CE (Jackson et al., 2000). Although the WPA is no longer present in the modern field, it remains identifiable in 10 ka time-averaged field models, where it shows even stronger inclination anomalies than the SAA (Constable et al., 2016). This feature is also captured by the GGF100k model, whose time-averaged radial non-dipole component indicates persistent activity in the western Pacific over the past 30 kyr (Fig. 1b), although the extent of this anomaly in the southern South China Sea remains uncertain due to limited data coverage (Panovska et al., 2018). In addition, lower geomagnetic intensity than the axial dipole moment, recorded from southern China around 4107 BCE (Luo et al., 2025) and from Cambodia around 1200 CE (Cai et al., 2021),

provides further archaeological evidence supporting the recurrence of this anomaly.

The WPA may reflect a long-lived geodynamic feature controlled by lower mantle structure. Studies on the SAA have shown that persistent geomagnetic anomalies tend to recur in specific regions, likely due to interactions with thermochemical structures in the lowermost mantle, such as LLVPs (Terra-Nova et al., 2019). These LLVPs, characterized by higher temperatures, distinct chemical compositions and higher densities, may locally influence core convection and persist for millions of years (Engbers et al., 2024; Tarduno et al., 2015). Similar to the SAA, the WPA is located at the steep western boundary of a Pacific LLVP (He and Wen, 2012), where upwelling core flow may facilitate the formation of reversed flux patches. The equatorial western Pacific may thus represent a preferred location for sustained non-dipole activity. Nevertheless, a more complete reconstruction of the WPA's evolution will rely on the availability of additional high-resolution paleomagnetic data, which is essential for improving our understanding of both the development of similar geomagnetic anomalies and the deep Earth's dynamo processes.

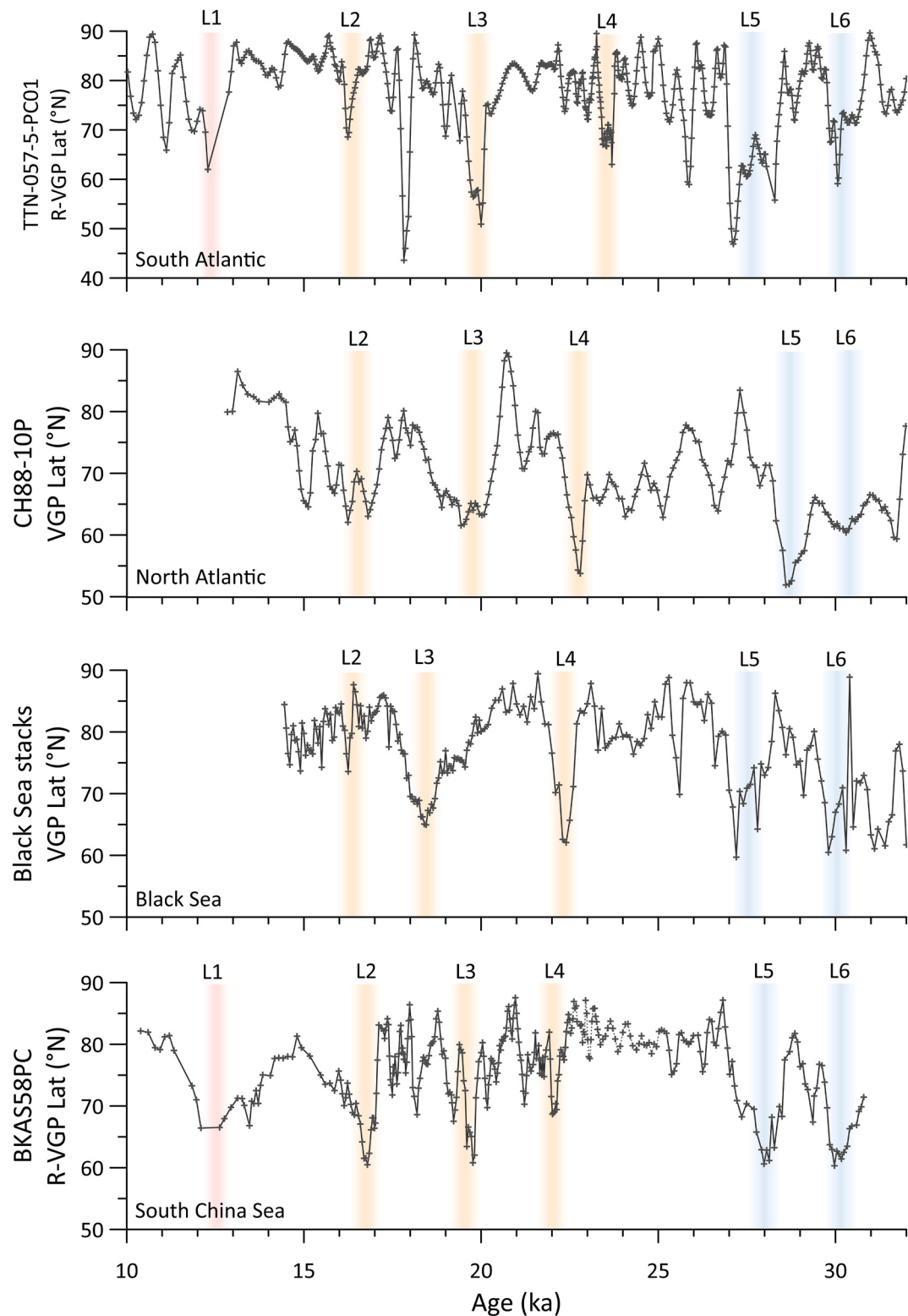


Fig. 11. Comparison of (R)VGP records from BKAS58PC with those from the Black sea (Liu et al., 2020), North Atlantic (Lund et al., 2005), and South Atlantic (Channell et al., 2000). As the BKAS58PC and cores 5-PC01 from the South Atlantic were not azimuthally oriented, the data represent relative directional variations. Colored bars mark corresponding low-latitude VGP intervals (L1-L6) across different records.

5. Conclusions

In this study, we present a high-resolution paleomagnetic record from core BKAS58PC in the southern South China Sea, addressing a critical gap in reconstructions of geomagnetic variability in this region

over the past 30 kyr. The record captures multiple low-latitude VGP swings between 30 and 10 ka, reflecting axial dipole instability during intervals of reduced field intensity following the Mono Lake excursion. Pronounced regional differences in relative paleointensity during 30–23 ka suggest enhanced non-dipole contributions during the recovery phase

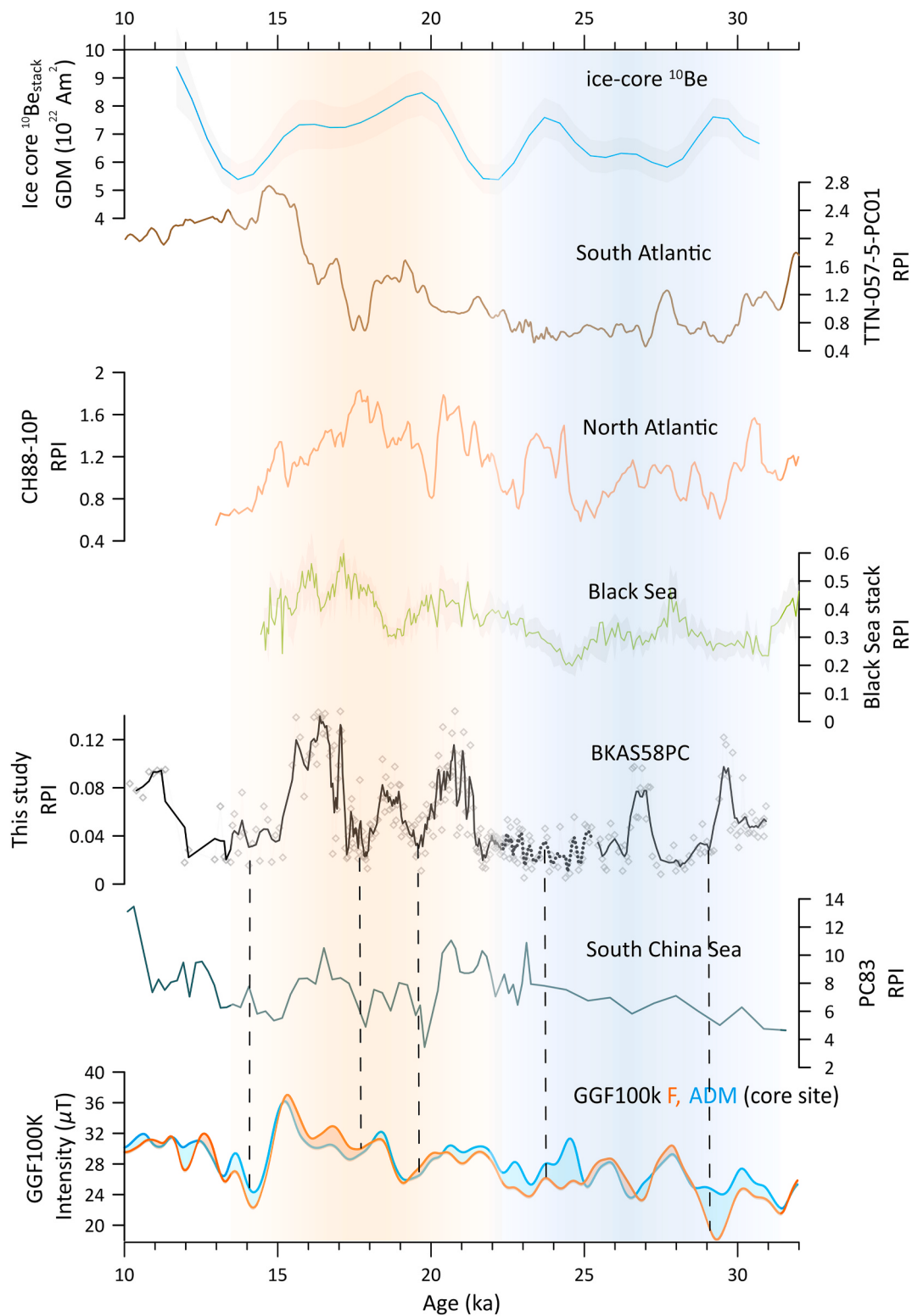


Fig. 12. Comparison of RPI results from core BKAS58PC with other regional and global records, including core PC83 from northern South China Sea (Yang et al., 2009), RPI stacks from the Black Sea (Nowaczyk et al., 2013), core 5-PC01 from the South Atlantic (Channel et al., 2000), core CH88-10P from the North Atlantic (Lund et al., 2005), the ^{10}Be stack-based reconstruction of the GDM from Greenland ice cores (Zheng et al., 2021), ADM values from the GGF100k model, and simulated geomagnetic field intensity (F) at the BKAS58PC core site (Panovska et al., 2018).

and may provide evidence for the past recurrence of the Western Pacific Anomaly. This new low-latitude record offers valuable insights into detailed geomagnetic field behavior and its links to deep Earth dynamics.

CRediT authorship contribution statement

Shuang Wu: Writing – original draft, Formal analysis, Investigation, Visualization. **Tingwei Zhang:** Writing – review & editing, Formal analysis, Investigation. **Xiaoqiang Yang:** Conceptualization,

Methodology, Funding acquisition, Resources, Writing – review & editing. **Shiyu Zhu:** Investigation. **Shengtan Shang:** Investigation. **Yulan Ye:** Investigation.

Formatting of funding sources

This research is supported by the projects of National Natural Science Foundation of China (42330504, 42274090).

Declaration of competing interest

The authors declare that they have no known competing financial interests or personal relationships that could have appeared to influence the work reported in this paper.

Appendix A. Supplementary data

Supplementary data to this article can be found online at <https://doi.org/10.1016/j.quascirev.2025.109611>.

Data availability

The paleomagnetic data used in this study are available at PANGAEA data repository via registration ([Wu and Yang, 2025](#)).

References

- Ahn, H.-S., Sohn, Y.K., Lee, J.-Y., Kim, J.C., 2018. Preliminary paleomagnetic and rock magnetic results from 17 to 22 ka sediment of Jeju Island, Korea: geomagnetic excursion behavior or rock magnetic anomalies? *Earth Planets Space* 70, 78. <https://doi.org/10.1186/s40623-018-0850-4>.
- Brachfeld, S.A., Banerjee, S.K., 2000. A new high-resolution geomagnetic relative paleointensity record for the North American Holocene: a comparison of sedimentary and absolute intensity data. *J. Geophys. Res. Solid Earth* 105, 821–834. <https://doi.org/10.1029/1999JB900365>.
- Cai, S., Doctor, R., Tauxe, L., Hendrickson, M., Hua, Q., Leroy, S., Phon, K., 2021. Archaeomagnetic results from Cambodia in Southeast Asia: evidence for possible low-latitude flux expulsion. *Proc. Natl. Acad. Sci.* 118, e2022490118. <https://doi.org/10.1073/pnas.2022490118>.
- Campuzano, S.A., Gómez-Páccard, M., Pavón-Carrasco, F.J., Osete, M.L., 2019. Emergence and evolution of the South Atlantic Anomaly revealed by the new paleomagnetic reconstruction SHAWQ2k. *Earth Planet Sci. Lett.* 512, 17–26. <https://doi.org/10.1016/j.epsl.2019.01.050>.
- Channell, J.E.T., Harrison, R.J., Lascu, I., McCave, I.N., Hibbert, F.D., Austin, W.E.N., 2016. Magnetic record of deglaciation using FORC-PCA, sortable-silt grain size, and magnetic excursion at 26 ka, from the Rockall Trough (NE Atlantic): a magnetic record of deglaciation. *G-cubed* 17, 1823–1841. <https://doi.org/10.1002/2016GC006300>.
- Channell, J.E.T., Singer, B.S., Jicha, B.R., 2020. Timing of Quaternary geomagnetic reversals and excursions in volcanic and sedimentary archives. *Quat. Sci. Rev.* 228, 106114. <https://doi.org/10.1016/j.quascirev.2019.106114>.
- Channell, J.E.T., Stoner, J.S., Hodell, D.A., Charles, C.D., 2000. Geomagnetic paleointensity for the last 100 kyr from the sub-antarctic South Atlantic: a tool for inter-hemispheric correlation. *Earth Planet Sci. Lett.* 175, 145–160. [https://doi.org/10.1016/S0012-821X\(99\)00285-X](https://doi.org/10.1016/S0012-821X(99)00285-X).
- Constable, C., Korte, M., Panovska, S., 2016. Persistent high paleosecular variation activity in southern hemisphere for at least 10 000 years. *Earth Planet Sci. Lett.* 453, 78–86. <https://doi.org/10.1016/j.epsl.2016.08.015>.
- Dahrin, D., Harlanti, U., Bijaksana, S., Kirana, K.H., Fajar, S.J., Suryanata, P.B., 2023. WEPAPIS 70 (Western Pacific paleointensity-stacking for the last 70 ka). *Quat. Sci. Rev.* 318, 108232. <https://doi.org/10.1016/j.quascirev.2023.108232>.
- de Oliveira, W.P., Hartmann, G.A., Terra-Nova, F., Pasqualon, N.G., Savian, J.F., Lima, E. F., da Luz, F.R., Trindade, R.I.F., 2024. Long-term persistency of a strong non-dipole field in the South Atlantic. *Nat. Commun.* 15, 9447. <https://doi.org/10.1038/s41467-024-53682-2>.
- Dunlop, D.J., 2002. Theory and application of the Day plot (Mrs/Ms versus Hcr/Hc) 1. Theoretical curves and tests using titanomagnetite data. *J. Geophys. Res.* 107, 2057. <https://doi.org/10.1029/2001JB000487>.
- Dunlop, D.J., Özdemir, Ö., 1997. Rock Magnetism: Fundamentals and Frontiers, first ed. Cambridge University Press. <https://doi.org/10.1017/CBO9780511612794>.
- Egli, R., 2004. Characterization of individual rock magnetic components by analysis of remanence curves. *Phys. Chem. Earth, Parts A/B/C* 29, 851–867. <https://doi.org/10.1016/j.pce.2004.04.001>.
- Elmaleh, A., Valet, J.-P., Herrero-Bervera, E., 2001. A map of the Pacific geomagnetic anomaly during the Brunhes chron. *Earth Planet Sci. Lett.* 193, 315–332. [https://doi.org/10.1016/S0012-821X\(01\)00518-0](https://doi.org/10.1016/S0012-821X(01)00518-0).
- Engbers, Y.A., Holme, R., Biggin, A.J., 2024. Miocene time-averaged geomagnetic field model suggests long lived mantle control and recurring structure in the South Atlantic. *Earth Planet Sci. Lett.* 626, 118535. <https://doi.org/10.1016/j.epsl.2023.118535>.
- Grinsted, A., Moore, J.C., Jevrejeva, S., 2004. Application of the cross wavelet transform and wavelet coherence to geophysical time series. *Nonlinear Process Geophys.* 11, 561–566. <https://doi.org/10.5194/npg-11-561-2004>.
- Harrison, R.J., Feinberg, J.M., 2008. FORCinel: an improved algorithm for calculating first-order reversal curve distributions using locally weighted regression smoothing. *G-cubed* 9. <https://doi.org/10.1029/2008GC001987>.
- He, F., Wei, Y., Maffei, S., Livermore, P.W., Davies, C.J., Mound, J., Xu, K., Cai, S., Zhu, R., 2021. Equatorial auroral records reveal dynamics of the paleo-West Pacific geomagnetic anomaly. *Proc. Natl. Acad. Sci.* 118, e2026080118. <https://doi.org/10.1073/pnas.2026080118>.
- He, Y., Wen, L., 2012. Geographic boundary of the “Pacific Anomaly” and its geometry and transitional structure in the north. *J. Geophys. Res. Solid Earth* 117. <https://doi.org/10.1029/2012JB009436>.
- Heaton, T.J., Köhler, P., Butzin, M., Bard, E., Reimer, R.W., Austin, W.E.N., Ramsey, C.B., Grootes, P.M., Hughen, K.A., Kromer, B., Reimer, P.J., Adkins, J., Burke, A., Cook, M. S., Olsen, J., Skinner, L.C., 2020. Marine 20—the marine radiocarbon age calibration curve (0–55,000 cal BP). *Radiocarbon* 62, 779–820. <https://doi.org/10.1017/RDC.2020.68>.
- Jackson, A., Jonkers, A.R.T., Walker, M.R., 2000. Four centuries of geomagnetic secular variation from historical records. *Philos. Trans. R. Soc. London, Ser. A: Math. Phys. Eng. Sci.* 358, 957–990. <https://doi.org/10.1098/rsta.2000.0569>.
- Jackson, M.J., Moskowitz, B., 2021. On the distribution of Verwey transition temperatures in natural magnetites. *Geophys. J. Int.* 224, 1314–1325. <https://doi.org/10.1093/gji/ggaa516>.
- Johnson, C.L., Constable, C.G., 1997. The time-averaged geomagnetic field: global and regional biases for 0–5 Ma. *Geophys. J. Int.* 131, 643–666. <https://doi.org/10.1111/j.1365-246X.1997.tb06604.x>.
- Johnson, C.L., Constable, C.G., 1995. The time-averaged geomagnetic field as recorded by lava flows over the past 5 Myr. *Geophys. J. Int.* 122, 489–519. <https://doi.org/10.1111/j.1365-246X.1995.tb07010.x>.
- Laj, C., Channell, J.E.T., 2015. Geomagnetic excursions. In: Schubert, G. (Ed.), *Treatise on Geophysics*, second ed. Elsevier, Oxford, pp. 343–383. <https://doi.org/10.1016/B978-0-444-53802-4.00104-4>.
- Laj, C., Kissel, C., Beer, J., 2004. High resolution global paleointensity stack since 75 kyr (GLOPIOS-75) calibrated to absolute values. In: *Timescales of the Paleomagnetic Field*. American Geophysical Union (AGU), pp. 255–265. <https://doi.org/10.1029/145GM19>.
- Laj, C., Kissel, C., Scafo, V., Beer, J., Thomas, D.M., Guillou, H., Muscheler, R., Wagner, G., 2002. Geomagnetic intensity and inclination variations at Hawaii for the past 98kyr from core SOH-4 (Big Island): a new study and a comparison with existing contemporary data. *Phys. Earth Planet. Inter.* 129, 205–243. [https://doi.org/10.1016/S0031-9201\(01\)00291-6](https://doi.org/10.1016/S0031-9201(01)00291-6).
- Laj, C., La j. C., Kissel, C., Mazaud, A., Channell, J.E.T., Beer, J., 2000. North Atlantic paleointensity stack since 75ka (NAPIS-75) and the duration of the Laschamp event. *Philos. Trans. R. Soc. London, Ser. A: Math. Phys. Eng. Sci.* 358, 1009–1025. <https://doi.org/10.1098/rsta.2000.0571>.
- Li, G., Rashid, H., Zhong, L., Xu, X., Yan, W., Chen, Z., 2018. Changes in deep water oxygenation of the South China sea since the last glacial period. *Geophys. Res. Lett.* 45, 9058–9066. <https://doi.org/10.1029/2018GL078568>.
- Liu, J., Nowaczyk, N., Frank, U., Arz, H., 2019. Geomagnetic paleosecular variation record spanning from 40 to 20 ka – implications for the Mono Lake excursion from Black Sea sediments. *Earth Planet Sci. Lett.* 509, 114–124. <https://doi.org/10.1016/j.epsl.2018.12.029>.
- Liu, J., Nowaczyk, N.R., Frank, U., Arz, H.W., 2018. A 20–15 ka high-resolution paleomagnetic secular variation record from Black Sea sediments – no evidence for the ‘Hilina Pali excursion’. *Earth Planet Sci. Lett.* 492, 174–185. <https://doi.org/10.1016/j.epsl.2018.04.014>.
- Liu, J., Nowaczyk, N.R., Jiang, X., Zhong, Y., Wirth, R., Liu, Q., Arz, H.W., 2022. Holocene paleosecular variations recorded by relict magnetic minerals in the Anoxic Black Sea sediments. *J. Geophys. Res. Solid Earth* 127, e2022JB024179. <https://doi.org/10.1029/2022JB024179>.
- Liu, J., Nowaczyk, N.R., Panovska, S., Korte, M., Arz, H.W., 2020. The Norwegian-Greenland sea, the laschamps, and the Mono Lake excursions recorded in a Black Sea sedimentary sequence spanning from 68.9 to 14.5 ka. *JGR Solid Earth* 125. <https://doi.org/10.1029/2019JB019225>.
- Liu, J., Xiang, R., Chen, Z., Chen, M., Yan, W., Zhang, L., Chen, H., 2013. Sources, transport and deposition of surface sediments from the South China Sea. *Deep Sea Res. Oceanogr. Res. Pap.* 71, 92–102. <https://doi.org/10.1016/j.dsr.2012.09.006>.
- Lougheed, B.C., Obrochta, S.P., 2019. A rapid, deterministic age-depth modeling routine for geological sequences with inherent depth uncertainty. *Paleoceanogr. Paleoclimatol.* 34, 122–133. <https://doi.org/10.1029/2018PA003457>.
- Lund, S.P., 2018. A new view of long-term geomagnetic field secular variation. *Front. Earth Sci.* 6. <https://doi.org/10.3389/feart.2018.00040>.
- Lund, S.P., Schwartz, M., Keigwin, L., Johnson, T., 2005. Deep-sea sediment records of the Laschamp geomagnetic field excursion (~41,000 calendar years before present). *J. Geophys. Res. Solid Earth* 110. <https://doi.org/10.1029/2003JB002943>.
- Lund, S.P., Schwartz, M., Stott, L., 2017. Long-term paleomagnetic secular variation and excursions from the western equatorial Pacific Ocean (MIS2-4). *Geophys. J. Int.* ggx029. <https://doi.org/10.1093/gji/ggx029>.
- Lund, S.P., Stott, L., Schwartz, M., Thunell, R., Chen, A., 2006. Holocene paleomagnetic secular variation records from the western Equatorial Pacific Ocean. *Earth Planet Sci. Lett.* 246, 381–392. <https://doi.org/10.1016/j.epsl.2006.03.056>.
- Luo, X., Liu, J., Wang, H., Schanner, M., Zhang, Y., Xie, P., Tang, J., Han, P., Li, Q., Han, F., Chen, X., Wen, C., Zhong, W., Hu, Y., Liu, Q., 2025. Low geomagnetic field

- intensity in southern China 6,000 Years ago. *Geophys. Res. Lett.* 52, e2024GL113552. <https://doi.org/10.1029/2024GL113552>.
- Necula, C., Lascu, I., Panaiotu, C., Gheorghe, D., 2024. Resolving the interpretation of magnetic coercivity components from backfield isothermal remanence curves using unmixing of non-linear Preisach maps: application to loess-paleosol sequences. *J. Geophys. Res. Solid Earth* 129, e2024JB029004. <https://doi.org/10.1029/2024JB029004>.
- Nowaczyk, N.R., Antonow, M., Knies, J., Spielhagen, R.F., 2003. Further rock magnetic and chronostratigraphic results on reversal excursions during the last 50 ka as derived from northern high latitudes and discrepancies in precise AMS 14C dating. *Geophys. J. Int.* 155, 1065–1080. <https://doi.org/10.1111/j.1365-246X.2003.02115.x>.
- Nowaczyk, N.R., Frank, U., Kind, J., Arz, H.W., 2013. A high-resolution paleointensity stack of the past 14 to 68 ka from Black Sea sediments. *Earth Planet Sci. Lett.* 384, 1–16. <https://doi.org/10.1016/j.epsl.2013.09.028>.
- Oliva, P., Viers, J., Dupré, B., 2003. Chemical weathering in granitic environments. *Chem. Geol.* 202, 225–256. <https://doi.org/10.1016/j.chemgeo.2002.08.001>.
- Panovska, S., Constable, C.G., Korte, M., 2018. Extending global continuous geomagnetic field reconstructions on timescales beyond Human Civilization. *G-cubed* 19, 4757–4772. <https://doi.org/10.1029/2018GC007966>.
- Pavón-Carrasco, F.J., De Santis, A., 2016. The South Atlantic anomaly: the key for a possible geomagnetic reversal. *Front. Earth Sci.* 4.
- Peck, J.A., King, J.W., Colman, S.M., Kravchinsky, V.A., 1996. An 84-kyr paleomagnetic record from the sediments of Lake Baikal, Siberia. *J. Geophys. Res. Solid Earth* 101, 11365–11385. <https://doi.org/10.1029/96JB00328>.
- Reilly, B.T., Stoner, J.S., Hatfield, R.G., Abbott, M.B., Marchetti, D.W., Larsen, D.J., Finkenbinder, M.S., Hillman, A.L., Kuehn, S.C., Heil, C.W., 2018. Regionally consistent Western North America paleomagnetic directions from 15 to 35 ka: assessing chronology and uncertainty with paleosecular variation (PSV) stratigraphy. *Quat. Sci. Rev.* 201, 186–205. <https://doi.org/10.1016/j.quascirev.2018.10.016>.
- Reimer, P.J., Reimer, R.W., 2001. A marine reservoir correction database and on-line interface. *Radiocarbon* 43, 461–463. <https://doi.org/10.1017/S003382200038339>.
- Roberts, A.P., Chang, L., Rowan, C.J., Horng, C.-S., Florindo, F., 2011. Magnetic properties of sedimentary greigite (Fe3S4): an update. *Rev. Geophys.* 49. <https://doi.org/10.1029/2010RG000336>.
- Roberts, A.P., Winklhofer, M., 2004. Why are geomagnetic excursions not always recorded in sediments? Constraints from post-depositional remanent magnetization lock-in modelling. *Earth Planet Sci. Lett.* 227, 345–359. <https://doi.org/10.1016/j.epsl.2004.07.040>.
- Sakuramoto, Y., Yamazaki, T., Kimoto, K., Miyairi, Y., Kuroda, J., Yokoyama, Y., Matsuzaki, H., 2017. A geomagnetic paleointensity record of 0.6 to 3.2 Ma from sediments in the western equatorial Pacific and remanent magnetization lock-in depth. *J. Geophys. Res. Solid Earth* 122, 7525–7543. <https://doi.org/10.1002/2017JB014450>.
- Singer, B.S., Jicha, B.R., He, H., Zhu, R., 2014. Geomagnetic field excursion recorded 17 ka at Tianchi Volcano, China: new 40Ar/39Ar age and significance. *Geophys. Res. Lett.* 41, 2794–2802. <https://doi.org/10.1029/2014GL059439>.
- Stoner, J.S., Channell, J.E.T., Mazaad, A., Strano, S.E., Xuan, C., 2013. The influence of high-latitude flux lobes on the Holocene paleomagnetic record of IODP Site U1305 and the northern North Atlantic. *G-cubed* 14, 4623–4646. <https://doi.org/10.1002/ggge.20272>.
- Stoner, J.S., Laj, C., Channell, J.E.T., Kissel, C., 2002. South Atlantic and North Atlantic geomagnetic paleointensity stacks (0–80 ka): implications for inter-hemispheric correlation. *Quaternary Science Reviews*, Decadal-to-Millennial-Scale Climate Variability 21, 1141–1151. [https://doi.org/10.1016/S0277-3791\(01\)00136-6](https://doi.org/10.1016/S0277-3791(01)00136-6).
- Stuiver, M., Reimer, P.J., 1993. Extended ^{14}C data base and revised CALIB 3.0 ^{14}C age calibration program. *Radiocarbon* 35, 215–230. <https://doi.org/10.1017/S003382200013904>.
- Tarduno, J.A., Watkeys, M.K., Huffman, T.N., Cottrell, R.D., Blackman, E.G., Wendt, A., Scribner, C.A., Wagner, C.L., 2015. Antiquity of the South Atlantic Anomaly and evidence for top-down control on the geodynamo. *Nat. Commun.* 6, 7865. <https://doi.org/10.1038/ncomms8865>.
- Tarling, D.H., Hrouda, F., 1993. *Magnetic Anisotropy of Rocks*.
- Tauxe, L., 1993. Sedimentary records of relative paleointensity of the geomagnetic field: theory and practice. *Rev. Geophys.* 31, 319–354. <https://doi.org/10.1029/93RG01771>.
- Terra-Nova, F., Amit, H., Choblet, G., 2019. Preferred locations of weak surface field in numerical dynamos with heterogeneous core–mantle boundary heat flux: consequences for the South Atlantic Anomaly. *Geophys. J. Int.* 217, 1179–1199. <https://doi.org/10.1093/gji/ggy519>.
- Terra-Nova, F., Amit, H., Hartmann, G.A., Trindade, R.I.F., 2016. Using archaeomagnetic field models to constrain the physics of the core: robustness and preferred locations of reversed flux patches. *Geophys. J. Int.* 206, 1890–1913. <https://doi.org/10.1093/gji/ggw248>.
- Terra-Nova, F., Amit, H., Hartmann, G.A., Trindade, R.I.F., 2015. The time dependence of reversed archeomagnetic flux patches. *J. Geophys. Res. Solid Earth* 120, 691–704. <https://doi.org/10.1002/2014JB011742>.
- Walczak, M.H., Stoner, J.S., Mix, A.C., Jaeger, J., Rosen, G.P., Channell, J.E.T., Heslop, D., Xuan, C., 2017. A 17,000 yr paleomagnetic secular variation record from the southeast Alaskan margin: regional and global correlations. *Earth Planet Sci. Lett.* 473, 177–189. <https://doi.org/10.1016/j.epsl.2017.05.022>.
- Wilkin, R.T., Barnes, H.L., 1997. Formation processes of frambooidal pyrite. *Geochem. Cosmochim. Acta* 61, 323–339. [https://doi.org/10.1016/S0016-7037\(96\)00320-1](https://doi.org/10.1016/S0016-7037(96)00320-1).
- Wilkin, R.T., Barnes, H.L., Brantley, S.L., 1996. The size distribution of frambooidal pyrite in modern sediments: an indicator of redox conditions. *Geochem. Cosmochim. Acta* 60, 3897–3912. [https://doi.org/10.1016/0016-7037\(96\)00209-8](https://doi.org/10.1016/0016-7037(96)00209-8).
- Wilson, R.L., 1970. Permanent aspects of the Earth's non-dipole magnetic field over upper tertiary times. *Geophys. J. Int.* 19, 417–437. <https://doi.org/10.1111/j.1365-246X.1970.tb06056.x>.
- Wu, S., Yang, X., 2025. Paleomagnetic records of core BKASS8PC from the southern South China Sea. PANGAEA. <https://doi.org/10.1594/PANGAEA.980749>.
- Yamazaki, T., Abdeldayem, A.L., Ikebara, K., 2003. Rock-magnetic changes with reduction diagenesis in Japan Sea sediments and preservation of geomagnetic secular variation in inclination during the last 30,000 years. *Earth Planets Space* 55, 327–340. <https://doi.org/10.1186/BF03351766>.
- Yamazaki, T., Ioka, N., 1997. Cautionary note on magnetic grain-size estimation using the ratio of ARM to magnetic susceptibility. *Geophys. Res. Lett.* 24, 751–754. <https://doi.org/10.1029/97GL00602>.
- Yamazaki, T., Kanamatsu, T., 2007. A relative paleointensity record of the geomagnetic field since 1.6 Ma from the North Pacific. *Earth Planets Space* 59, 785–794. <https://doi.org/10.1186/BF03352741>.
- Yamazaki, T., Kanamatsu, T., Mizuno, S., Hokanishi, N., Gaffar, E.Z., 2008. Geomagnetic field variations during the last 400 kyr in the western equatorial Pacific: paleointensity-inclination correlation revisited. *Geophys. Res. Lett.* 35. <https://doi.org/10.1029/2008GL035373>.
- Yamazaki, T., Li, J., Shimono, T., Kanamatsu, T., 2023. Difference in relative paleointensity recording efficiency of magnetic mineral constituents in a sediment core off Chile. *J. Geophys. Res. Solid Earth* 128, e2023JB026816. <https://doi.org/10.1029/2023JB026816>.
- Yamazaki, T., Oda, H., 2002. Orbital influence on Earth's magnetic field: 100,000-year periodicity in inclination. *Science* 295, 2435–2438. <https://doi.org/10.1126/science.1068541>.
- Yang, T., Dekkers, M.J., Zhao, X., Petronotis, K.E., Chou, Y.-M., 2022. Greigite Formation modulated by turbidites and bioturbation in deep-sea sediments offshore Sumatra. *J. Geophys. Res. Solid Earth* 127, e2022JB024734. <https://doi.org/10.1029/2022JB024734>.
- Yang, X., Heller, F., Nengyou, W., Jie, Y., Zhihua, S., 2009. Geomagnetic paleointensity dating of South China Sea sediments for the last 130 kyr. *Earth Planet Sci. Lett.* 284, 258–266. <https://doi.org/10.1016/j.epsl.2009.04.035>.
- Yang, X., Su, Z., Wei, G., Zhang, T., Chen, Q., Ye, Y., 2024. Geomagnetic paleointensity variations in the northern South China Sea since the late Pleistocene. *Quat. Sci. Rev.* 324, 108452. <https://doi.org/10.1016/j.quascirev.2023.108452>.
- Zhang, Y.G., Ji, J., Balsam, W.L., Liu, L., Chen, J., 2007. High resolution hematite and goethite records from ODP 1143, South China Sea: Co-evolution of monsoonal precipitation and El Niño over the past 600,000 years. *Earth Planet Sci. Lett.* 264, 136–150. <https://doi.org/10.1016/j.epsl.2007.09.022>.
- Zheng, M., Sturevik-Storm, A., Nilsson, A., Adolphi, F., Aldahan, A., Possnert, G., Muscheler, R., 2021. Geomagnetic dipole moment variations for the last glacial period inferred from cosmogenic radionuclides in Greenland ice cores via disentangling the climate and production signals. *Quat. Sci. Rev.* 258, 106881. <https://doi.org/10.1016/j.quascirev.2021.106881>.
- Zhong, Y., Liu, Y., Yang, X., Zhang, J., Liu, Jiabo, Bosin, A., Gorbarenko, S.A., Shi, X., Chen, T., Chou, Y.-M., Liu, W., Wang, H., Gai, C., Liu, Jianxing, Derkachev, A.N., Qiang, X., Liu, Q., 2020. Do non-dipole geomagnetic field behaviors persistently exist in the subarctic Pacific Ocean over the past 140 ka? *Science Bulletin* 65, 1505–1507. <https://doi.org/10.1016/j.scib.2020.05.016>.